

PILLAR-SUPPORTED PLASMONIC NANOANTENNAS FOR OPTICAL
NANOTWEEZERS AND OPTICAL AUDIO APPLICATIONS

BY

QING DING

THESIS

Submitted in partial fulfillment of the requirements
for the degree of Master of Science in Electrical and Computer Engineering
in the Graduate College of the
University of Illinois at Urbana-Champaign, 2017

Urbana, Illinois

Adviser:

Associate Professor Kimani Toussaint, Jr.

Abstract

Optical tweezers utilize momentum transfer from confined electromagnetic fields within micro- and nanoscale objects to form non-invasive probes that serve to provide piconewton forces and detect motion with angstrom-level precision. This technique was discovered in the 1980s and has been found useful in a variety of research fields. However, optical tweezers, based on the use of high-numerical aperture objective lenses, suffer the diffraction limit, which hampers investigation on objects of interest on smaller scale. With sub-diffraction field confinement and enhancement properties, metallic nanostructures offer an alternative approach to bypass the diffraction limit, making a promising candidate for tools that help research on nanoscale systems. The intensity gradients produced within the nanometer-sized gaps of plasmonic bowtie nanoantennas (BNAs) are orders of magnitude larger than those of conventional optical tweezers. Accordingly, plasmon-enhanced gradient forces can both significantly relax constraints for microparticle manipulation and offer a route for improved nanoparticle trapping.

This thesis explores the near-field enhancement and confinement properties of arrays of pillar-supported Au bowtie nanoantennas (pBNAs), a new type of bowtie nanoantenna that evolves from its previous substrate-bound version, for plasmonic optical trapping and plasmonic film application. Compared to their precursors, the pBNAs exhibit larger field enhancement and thus steeper intensity gradient, which facilitates the particle trapping to a greater extent. In addition, by extending the metallic nanoantennas into a three-dimensional geometry, the heating effect originating from the strong intrinsic absorption property of the metallic structure leads to a tremendous increment in temperature. This thermal effect can be utilized to locally modify the morphological shape of pBNAs, resulting in interesting optical response from the arrays of pBNAs. This optical response allows the pBNAs to provide a film platform for recording information like audio signals, in either the time or frequency domain, with the capability of performing signal processing on chip.

Acknowledgments

First, I want to thank my advisor Prof. Kimani Toussaint, Jr. He offered me the opportunity to conduct research with freedom on nano-optics in the PROBE lab. We had many discussions that not only inspired my research but also guided me through my personal life. I would also like to thank Dr. Gabriel Spalding for leading me into the world of optics, and Dr. Hao Chen for sharing his tremendous experience and knowledge in optics with me.

I have been pursuing higher education in Illinois for almost a decade. Without my family's support, I would not be the person I am today. Special thanks to my mother, Guolan Li. I cannot be more grateful for her consistent patience, understanding and support.

Contents

1. Introduction.....	1
2. Background and Theory.....	2
2.1 Electromagnetics	2
2.2 Drude-Sommerfeld Model	2
2.3 Interband Transition	3
2.4 Surface Plasmon Polaritons (SPPs).....	4
2.5 Localized Surface Plasmon Resonance (LSPRs)	5
3. Applications of Plasmonic Nanoantennas	6
3.1 Optical Antennas	6
3.2 Optical Trapping	7
3.2.1 Conventional Optical Trapping.....	7
3.2.2 Plasmonic Optical Trapping	8
3.2.3 Experimental Setup.....	11
3.2.4 Single Particle Plasmonic Optical Trapping	12
3.2.5 Multiple Particle Plasmonic Optical Trapping	14
3.2.6 Optical Guiding with Writable Channels.....	15
3.3 Optical Film and Audio Recording	17
4. Conclusion	25
References	26

1. Introduction

Plasmonics is the study of the interaction of metals with electromagnetic radiation. The background information and basic concepts of plasmonics will be briefly discussed first. The concept of optical antennas is introduced to describe devices enabling the control and manipulation of optical fields at the nanometer scale. The plasmonic effect was initially utilized on colloidal metallic particles accompanied by enhanced electromagnetic fields. It turns out that gap antennas, such as bowtie nanoantennas investigated by our lab, called the BNAs, have the capability of stronger subwavelength confinement of electromagnetic radiation within the gap region, creating a sharp gradient of optical field for potential application such as optical nanotweezers.

In terms of my research, I have been fortunate to work on a newer structure called the pBNAs consisting of bowtie nanoantenna arrays standing on SiO_2 pillars. The pBNAs exhibit stronger plasmonic response that leads to film effect which we can use to record audio signal and perform simple signal processing. More recently, we have demonstrated a novel etching technique named the plasmon-assisted etching of the pBNAs. It has motivated us to use it for fabricating planar optical components, and as a proof-of-concept, the examples of fabricated planar optical components in our lab will be presented, followed by the summary of my work in the conclusion.

2. Background and Theory

2.1 Electromagnetics

To understand plasmonics and its corresponding optical properties, we need to review the governing equations that describe these light-matter interactions, which in essence are the interactions between nanoscale structures and time-harmonic electromagnetic fields. These equations are Maxwell's equations, which express the relationship between the electric (\mathbf{E}) and magnetic (\mathbf{H}) field [1]:

$$\nabla \times \mathbf{E} = -i\omega\mathbf{B}, \quad (2.1)$$

$$\nabla \times \mathbf{H} = i\omega\mathbf{D} + \mathbf{J}, \quad (2.2)$$

$$\nabla \cdot \mathbf{D} = \rho, \quad (2.3)$$

$$\nabla \cdot \mathbf{B} = 0, \quad (2.4)$$

where i is the imaginary unit, ω is the angular frequency, and \mathbf{J} and ρ are the spatial current and charge densities, respectively. The relationship between the electric and magnetic fields and the electric displacement (\mathbf{D}) and magnetic induction (\mathbf{B}) is given as

$$\mathbf{D} = \varepsilon_0\mathbf{E} + \mathbf{P}, \quad (2.5)$$

$$\mathbf{B} = \mu\mathbf{H}, \quad (2.6)$$

where ε and μ are the electric permittivity and magnetic permeability of the material, respectively. Depending on the material-dependent relative permittivity ε_r and permeability μ_r , we have $\varepsilon = \varepsilon_0\varepsilon_r$ and $\mu = \mu_0\mu_r$, where $\varepsilon_0 = 8.854 \times 10^{-12}$ F/m is the vacuum permittivity and $\mu_0 = 4\pi \times 10^{-7}$ H/m is the vacuum permeability [1]. The material-dependent relative permittivity is given by $\varepsilon_r = 1 + \chi_e$ and χ_e is the dielectric susceptibility of the medium. Thus, the polarization of the medium can be written as $\mathbf{P} = \varepsilon_0 \chi_e \mathbf{E}$ and the electric displacement can be written as $\mathbf{D} = \varepsilon_0 \mathbf{E} + \varepsilon_0 \chi_e \mathbf{E} = \varepsilon_0 \varepsilon_r \mathbf{E} = \varepsilon \mathbf{E}$ [1]. The relationship between the current density and the electric field is given by $\mathbf{J} = \sigma \mathbf{E}$, where σ is the conductivity of the material.

2.2 Drude-Sommerfeld Model

The interaction between metals and light is the phenomenon that is mainly dictated by the free conduction electrons in the metal. According to the simple Drude model, the free electrons

oscillate 180° out of phase relative to the driving electric field. Therefore, most metals possess a negative dielectric constant at optical frequencies which leads to a very high reflectivity. Furthermore, the free electron gas within metals driven at optical frequencies can possess surface and volume charge density oscillations, defined as plasmon polaritons or plasmons with unique resonance frequencies.

To describe such interaction, the simple Drude model is applied as an initial attempt to explain plasmons. Assuming free-electron gas driven by certain electric field with amplitude \mathbf{E}_0 and frequency ω , the motion of electrons is given as [1]

$$m_e \frac{\partial^2 \mathbf{r}}{\partial t^2} + m_e \Gamma \frac{\partial \mathbf{r}}{\partial t} = e \mathbf{E}_0 e^{-i\omega t}, \quad (2.7)$$

where e and m_e are the charge and the effective mass of the free electrons. No restoring force is considered with the assumption of free electrons. The damping term is proportional to Γ , which is defined by the Fermi velocity over the electron mean free path between scattering events. Solving Eq. 2.7 with the expression of material-dependent relative permittivity, the dielectric function given by the Drude model yields

$$\epsilon_{\text{Drude}}(\omega) = 1 - \frac{\omega_p^2}{\omega^2 + \Gamma^2} + i \frac{\Gamma \omega_p^2}{\omega(\omega^2 + \Gamma^2)}. \quad (2.8)$$

In Eq. 2.8, ω_p is called the volume plasma frequency, which is a constant. Apparently, the dielectric function contains a real and imaginary part. The real part is negative, meaning that light can penetrate a metal only to a very small extent, and also leads to a strong imaginary part of the refractive index, which is associated with energy dissipation that is connected with the electron motion in the metal.

2.3 Interband Transition

The Drude model only takes the free electron gas into account; however, the response of bound electrons can also contribute to the overall optical interaction between metal and electromagnetic fields. For instance, when the wavelength of light decreases to less than 550 nm, the higher-energy photons are able to excite electrons from the valence band into the conduction band. From a classical perspective, the motion of bound electrons can be viewed by

$$m \frac{\partial^2 \mathbf{r}}{\partial t^2} + m\gamma \frac{\partial \mathbf{r}}{\partial t} + \alpha \mathbf{r} = e \mathbf{E}_0 e^{-i\omega t}, \quad (2.9)$$

where m is the effective mass of the bound electrons, γ is the damping constant associated with mainly radiative damping, and α is the spring constant of the potential of the bound electron. Similar to the Drude model, the dielectric function can be solved from Eq. 2.9 and written with the real and imaginary parts

$$\varepsilon_{\text{Interband}}(\omega) = 1 - \frac{\tilde{\omega}_p^2(\omega_0^2 - \omega^2)}{(\omega_0^2 - \omega^2)^2 + \gamma^2 \omega^2} + i \frac{\gamma \tilde{\omega}_p^2 \omega}{(\omega_0^2 - \omega^2)^2 + \gamma^2 \omega^2}. \quad (2.10)$$

In Eq. 2.10, $\tilde{\omega}_p$ is the modified plasma frequency in analogy to that in the Drude-Sommerfeld model, and $\omega_0 = \sqrt{\alpha/m}$. For wavelength below 650 nm, the interband transitions become significant. However, as the wavelength continues decreasing to below 500 nm, higher-energy interband transitions become significant and are no longer accurately predicted by the model here since only one interband transition is taken into account in this particular case [1].

2.4 Surface Plasmon Polaritons (SPPs)

Surface plasmons are the collective oscillations in the electron density at the surface of a metal. The surface charge oscillations are coupled to electromagnetic waves. A combined excitation consisting of a surface plasmon and a photon is called a surface plasmon polariton. Consider a plane interface between two media, one having a complex frequency-dependent dielectric function $\varepsilon_1(\omega)$ and the other having a real dielectric function $\varepsilon_2(\omega)$. If the interface is at the plane $z = 0$, the electric field of the surface polariton propagating at the interface ($z = 0$) in the x -direction can be expressed as [2]

$$\mathbf{E}_{\text{sp}}(x, z) = \mathbf{E}_0 e^{ik_{\text{sp}}x - k_z|z|}. \quad (2.11)$$

This field suggests a surface plasmon mode propagating along the interface with wavevector k_{sp} and exponentially decaying from the interface with decay constant k_z . The wavevector k_{sp} and normal component k_z is given as

$$k_{\text{sp}}^2 = \left(\frac{\omega}{c}\right)^2 \frac{\varepsilon_1 \varepsilon_2}{\varepsilon_1 + \varepsilon_2}, k_{j,z}^2 = \left(\frac{\omega}{c}\right)^2 \frac{\varepsilon_j^2}{\varepsilon_1 + \varepsilon_2} (j = 1, 2). \quad (2.12)$$

In order to have a sustainable solution, the normal component has to be purely imaginary in both media giving rise to exponentially decaying solutions. The following conditions must be satisfied:

$$\varepsilon_1(\omega) \cdot \varepsilon_2(\omega) < 0, \quad (2.13)$$

$$\varepsilon_1(\omega) + \varepsilon_2(\omega) < 0, \quad (2.14)$$

meaning that the SPPs can exist only at the metal-dielectric interface, where a metal has large negative real part of the dielectric constant [1].

2.5 Localized Surface Plasmon Resonance (LSPR)

In addition to SPPs, the second fundamental excitation of plasmonics is called localized surface plasmons, which are non-propagating excitations of the conduction electrons of metallic nanostructures coupled to the electromagnetic field. If a spherical metallic particle of size a is much smaller than the wavelength of light, a quasi-static approximation can be applied to solve for the electric field inside and outside the particle

$$\mathbf{E}_{in} = \mathbf{E}_0 \frac{3\varepsilon_m}{\varepsilon + 2\varepsilon_m}, \quad (2.15)$$

$$\mathbf{E}_{out} = \mathbf{E}_0 + \frac{3\mathbf{n}(\mathbf{n} \cdot \mathbf{p}) - \mathbf{p}}{4\pi\varepsilon_0\varepsilon_m} \frac{1}{r^3}, \quad (2.16)$$

where \mathbf{p} is the induced oscillating dipole moment

$$\mathbf{p} = \varepsilon_0\varepsilon_m\alpha\mathbf{E}_0, \quad (2.17)$$

and the polarizability is

$$\alpha = 4\pi a^3 \frac{\varepsilon - \varepsilon_m}{\varepsilon + 2\varepsilon_m}. \quad (2.18)$$

Apparently, the polarizability of the metallic nanoparticle experiences a resonant enhancement under the circumstance that $|\varepsilon + 2\varepsilon_m|$ is a minimum, simply $\text{Re}[\varepsilon(\omega)] = -2\varepsilon_m$. This relationship is called the Fröhlich condition, and the associated mode is called the dipole surface plasmon of the metal nanoparticle. The surface plasmon resonance is largely dictated by α and so is the resonant enhancement of both internal and external fields. This field-enhancement is the key to many applications of metal nanoparticles in optical devices and sensors [1, 3].

3. Applications of Plasmonic Nanoantennas

3.1 Optical Antennas

Analogous to microwave and radio-wave antennas, optical antennas are a kind of nanostructure for manipulating and controlling optical radiation at subwavelength scales. They are defined as devices designed to efficiently convert free-propagating optical radiation to localized energy, and vice versa [1]. However, there are crucial differences between optical antennas and their precursors, mainly due to the fact that metals are lossy at optical frequencies. In the regime of optical frequencies, optical antennas are essentially strongly correlated plasmas described as a free electron gas. Under excitation of optical frequencies, the free electrons in a metal give rise to collective motion. These charge density oscillations are characterized as surface plasmon resonance, and normally take place in noble metals like Au and Ag at the optical to IR wavelengths [4].

As discussed in earlier context, there are two major forms in which surface plasmons occur: (1) surface plasmon polaritons (SPPs) and (2) localized surface plasmon resonances (LSPRs). The SPPs are propagating modes where the surface plasmon travels along a metal-dielectric interface and has an evanescent decay from the surface. The excitation of SPPs requires phase matching with the excitation field, which is normally fulfilled by prism or grating coupling. In contrast, LSPRs are non-propagating modes that take place in a 2D field confinement, such as a nanowire, or a 3D field confinement, such as a spherical particle. In the context of my research, only LSPR will be discussed since it is the major surface plasmon resonance associated with our plasmonic nanostructures. For a small subwavelength-scale particle such as a single antenna made by a spherical particle or linear rod, the electron gas is highly confined within and this extreme local charge accumulation leads to enhanced optical fields. What is more, for gap antennas, the optical fields can be highly confined and thus strongly enhanced within the designed gap region. By arranging these gap antennas in arrays, additional array resonance can be introduced to further increase the field enhancement in the gap by an order of magnitude [5].

As a specific type of gap antennas, the bowtie nanoantennas in our lab consist of tip-to-tip gold triangles with a feed gap in between. The feature of larger aspect ratios of BNAs allows the lightning rod effect near the sharp tips with field enhanced by an order of magnitude. It has been demonstrated that the parameters of BNAs, such as the radius of curvature, the gap size and side

dimensions, can be tuned with efficient coupling to engineer the total field enhancement in the gap on the order of 10^4 . Our BNA samples are fabricated via e-beam lithography in $80 \times 80 \mu\text{m}^2$ regions with various array spacings (425, 475, 525 and 575 nm). As illustrated in Fig. 1, a gold layer is deposited after a 5 nm adhesion layer, normally Ti and Cr, on an ITO-coated glass substrate. By default, the horizontal direction is set as the x-axis while the vertical direction is set as the y-axis.

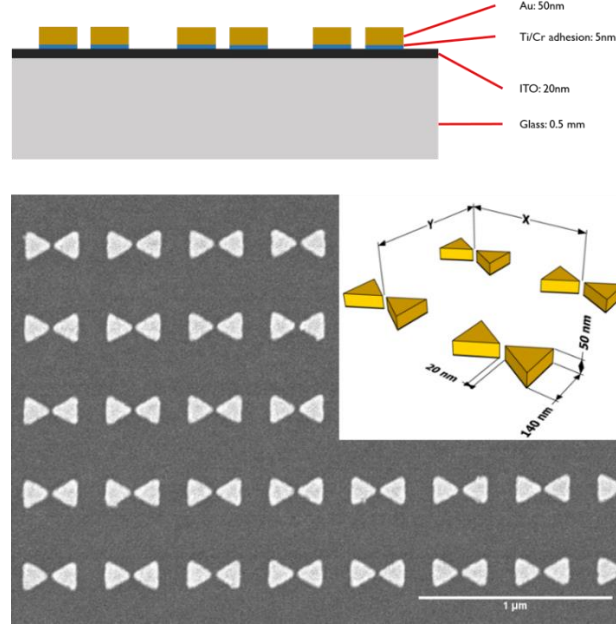


Figure 1. Design schematic and SEM of BNAs [6].

As a consequence of strong field enhancement, large field gradient is present near the gap regions of BNAs, which can be exploited to generate enhanced gradient force for applications like manipulation of particles.

3.2 Optical Trapping

3.2.1 Conventional Optical Trapping

It is easier to visualize how optical trapping works with ray-optics analysis in the Mie regime. This approach offers an intuitive picture of the optical forces generated by reflection and refraction of rays.

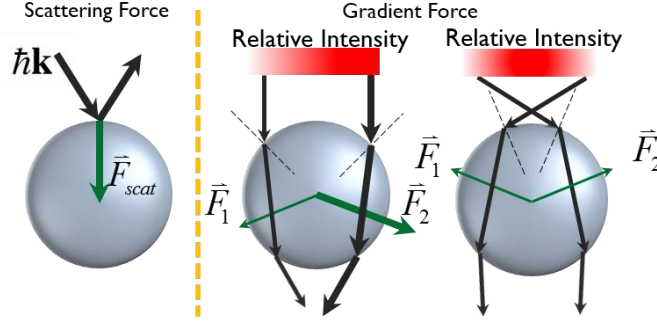


Figure 2. The ray-optics analysis in the Mie regime for optical trapping [7].

The scattering force arises from reflection of incident rays from the particle surface, which causes a net downstream force on the particle. For a particle with a refractive index larger than that of its surrounding, the refraction of the rays by the bead changes the momentum of the photons, equal to the change in the direction of the input and output rays. Following the conservation of momentum, the bead acquires momentum with equal but opposite amount, which results in the forces depicted by the green arrows in Fig. 2. With different incident intensities, the particle is pulled towards the higher intensity. To form a stable trap, the focused light is a must, so that three-dimensional intensity gradient can be achieved. In this situation, the bead is illuminated by a focused beam of light with a radial intensity gradient. Two rays are again refracted by the bead but the change in momentum in this instance leads to a net force towards the focus. The lateral forces balance each other out and the axial force is balanced by the scattering force [7]. To satisfy those conditions, conventional optical trapping requires a high-NA objective and quality spatial intensity distribution. In contrast, the enhanced field gradient brought by the BNAs can boost the gradient force so that the demand for a high-NA objective and spatial mode quality is alleviated. Experimentally, it has been demonstrated that the BNAs are sufficient to perform all-around efficient tweezing on single particle, multiple particles and particle stacking [8].

3.2.2 Plasmonic Optical Trapping

Plasmonic nanotweezers based on localized surface plasmon resonance (LSPR) excited in metallic nanostructures continue to attract increased attention due to the generation of highly enhanced electric fields with sub-diffraction spatial confinement [9, 10]. This localized field in a nanoscale system results in a large intensity gradient which is responsible for a large optical trapping force being able to produce a better trapping performance compared to the conventional

counterparts based on focused light in free space. Instead of micro-sized object trapping, plasmonic nanotweezers can be utilized for nanoscale particle trapping and metallic particle trapping which is difficult to achieve by conventional optical tweezers due to the inherent diffraction limit [11]. As an important tool for near field optical manipulation, plasmonic nanotweezers based on nanoscale system can be easily integrated in a compact lab-on-chip system and many clinical and daily life applications can be realized.

It is common sense that appropriately designed nanoantennas are able to produce “hot spots” where the incident electromagnetic field is enhanced by several orders of magnitude when resonantly pumped. Once an optical device with specially designed nanostructures is fabricated, a valid working wavelength range centered at a certain wavelength of resonance is decided [8, 12]. The tunability of postprocess is less due to lack of effective approaches to alter the shape of nanostructure. In this thesis, we present a writable plasmonic platform of Au bowtie nanoantenna (BNA) array supported on SiO₂ pillars which is able to record the near-field optical intensity. Here, we refer to this system as “plasmonic film” [13]. Photothermally induced morphological changes in the BNAs on pillars (pBNAs) cause a tunable spectral response of 50 nm in the visible region. Measurement for the optical trapping ability is carried out to study the influence of the spectral response changes. It is shown that the unexposed plasmonic film with the smallest gap size demonstrates the largest trapping stiffness and a gradual decrease is observed for the increased laser power dosage. Though the trapping ability is degraded, the plasmonic film is still active and functional. We also present a subtle multiple particle trapping on the unexposed plasmonic film with a very weak input power density using a 0.25 numerical aperture (NA) objective. Based on the given tunability and designable platform, an arbitrarily designed pattern is written on the film. As the difference of trapping ability gives rise to a preferred trapping channel, multiple particles are moved by an approximately collimated optical beam and followed the trajectory of the channel which enables passive particle sorting in an optofluidic channel “without walls”.

The functionality of plasmonic film is derived from photo-thermally induced morphological changes in the Au particles. The plasmonic film of pBNAs is a photo-sensitive film at resonant wavelength. A dramatic temperature increase results from formation of a strong localized field at the tip of the bowtie structure when resonantly pumped [14]. Unlike our previous setting in

which the BNAs are placed on top of the substrate [12], the pBNA would not experience limitation of field enhancement and the ITO layer would not be in contact with the metallic nanostructure preventing the melting effect. Though the temperature increase in this system is below the bulk melting temperature of Au (1067 °C), surface melting is enhanced at the sharp tip and can occur at temperatures lower than the melting temperature. And this enhanced temperature increase of pBNA is more than 10x higher than that of traditional substrate-bound BNAs [12]. Thus, under the right illumination conditions, the radius of curvature of the nanoantennas can be increased from ~15 to ~20 nm [12], along with a concomitant increase in the gap spacing that separates the Au triangle pairs that form each bowtie nanoantenna; moreover, the height or thickness of each triangle is also reduced. All of these shape changes significantly influence the spectral response of the nanostructure (in this case, blue-shifted). Given an input power, the nanostructure tends to shrink and the resonance wavelength is shifted. As a result, the input wavelength becomes off-resonance, and then the surface melting phenomenon stops. The greater the power density, the more the spectral shift restores the system back to the balanced point. Under this mechanism, by careful measurement of the spectrum, it is possible to record the laser power writing on the film and vice versa.

Heating of the pBNAs is generated by focusing a wavelength 660 nm, CW laser onto the nanostructures with a collar adjustable, 0.6 (NA) objective (Olympus LUCplanFLN 40×), which produces a focal spot with radius of approximately 670 nm; the laser is polarized along the long axis of the antenna, which is referred to as horizontal polarization. As the input power is increased from 500 μW to 2 mW, which corresponds to dosages from 0 to 1.4 $\text{mW}\cdot\mu\text{m}^{-2}$, the color of the exposed region visibly changes from light green to red (Fig. 3a)[15]. The optical response of each $\sim 22 \times 22 \mu\text{m}$ block of the exposed film is assessed by measuring the spectral reflectance R . A spatially coherent, supercontinuum source is focused onto the modified regions. The supercontinuum optical source derives from a photoniccrystal fiber (Femtowhite 800, NKT Photonics) pumped using a Ti:sapphire laser with 100 fs pulselength, 80 MHz pulse repetition rate, 800 nm center wavelength, and ~ 200 mW average power. The source is coupled into an optical microscope (IX-81, Olympus) equipped with the 0.6 NA objective and spectra are taken using a fiber-coupled spectrometer (USB-2000+, Ocean Optics). As the input laser dosage is increased from 0 to 1.4 $\text{mW}\cdot\mu\text{m}^{-2}$, the main LSPR shifts from 657 nm to 621 nm (Fig. 3b). To

verify the relationship between observed LSPR shifts and geometrical changes of the nanoantennas, we calculate theoretical power reflectance curves by modeling the exposed pBNAs using the observed structural changes, including radii of curvature, triangle height, or sphere radius (where applicable). Using plane wave excitation with normal incidence, the spectral location of the peak LSPR shows close correspondence with experimental data.

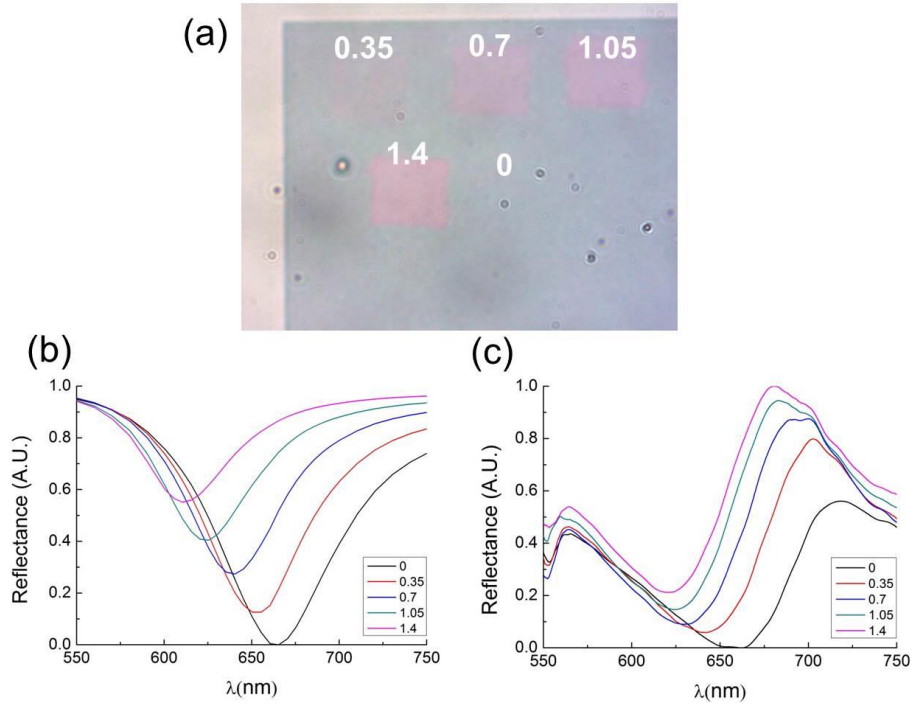


Figure 3. (a) Optical image of the plasmonic film showing the exposed area with dosage ranging from 0 to 1.4 mW/μm². (b) and (c) are experimental and theoretical spectral response. Plots demonstrate the plasmonic resonance as a function of dosage. Numbers represent the dosage in mW/μm² [16].

3.2.3 Experimental Setup

The experimental setup is detailed in Fig. 4. In the upright orientation, 425×425 nm spaced pBNAs are illuminated from the substrate side by a 0.6 numerical aperture (NA) objective at either non-resonant ($\lambda_{\text{or}}=660$ nm) or near resonant ($\lambda_{\text{nr}}=685$ nm) wavelengths with input polarization along the long axis of the bowtie and an input power range of 200 - 800 μW. The plasmonic nanotweezers are built around a customized inverted microscope (Olympus IX81) with a 0.6 NA, collar-adjustable microscope objective (Olympus LUCPlanFLN 40×) and a 0.65 NA, microscope objective (Olympus PlanN 40×). The latter one is used to collect scattered light from the trapped particle and sent to a quadrant photodetector. The pBNAs are fabricated in 80×80 μm² arrays with a lattice constant of 425 nm (center-to-center spacing). The excitation

source is a power tunable wavelength 660 nm or 685 nm CW source and coupled into the microscope via a horizontal polarizer. A halogen lamp, white light source (Dolan Jenner, 190) is used to image the particles (Duke Scientific) onto a CCD camera (Thorlabs, DCC1645C), which is preceded by a laser-blocking band-pass filter. Trapping chambers are made with a 13 mm diameter gasket (Ivitrogen CoverWell) sandwiched between two microscope coverslips (Corning). All particles used in the experiment are suspended in water and a typical concentration of 1:1000 is used. The strength of the nanotweezer is assessed by measuring the lateral trap stiffness with 1.0 μ m diameter silica bead (DukeScientific) as a function of laser power dosage.

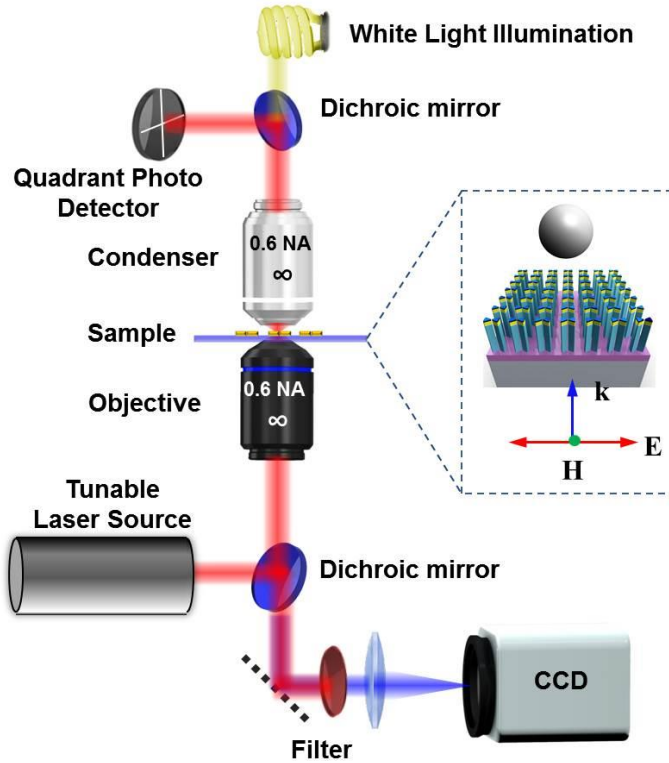


Figure 4. Schematic diagram of experimental setup [17]. The optical wave vector k , incident electric E and magnetic fields H are represented by blue, red, and green arrows, respectively [16].

3.2.4 Single Particle Plasmonic Optical Trapping

Figure 5a, b show the experimentally measured trapping stiffness for all parameters considered in this study. Figure 3c shows the absorption cross-section σ of an upright, single bowtie in a 425×425 nm array obtained by using commercial solver (COMSOL Multiphysics). The grid size of the simulation volume is set as $\lambda/20$, where λ is the wavelength of light. We note that the peak

of absorption cross section is at 791 nm and the laser wavelength we explore in this study is 660 nm and 685 nm. The latter one is close to the resonance and the previous one is off resonance. In general, we observe that the trapping stiffness is in a negative correlation with the laser power dosage in both cases, owing to the morphological changes of the nanostructure. As the gap size and radius of curvature are enlarged due to the photo-thermal induced melting, the localized field and trapping force decrease correspondingly. Moreover, the trapping stiffness for 660-nm wavelength is ranging from 1.41 to 3.03 $\text{pN}\cdot\mu\text{m}^{-1}\text{mW}^{-1}$, while the maximum value of stiffness for 685 nm is 1.31 $\text{pN}\cdot\mu\text{m}^{-1}\text{mW}^{-1}$. We see that non-resonant excitation of pBNAs provides greater stiffness than the near resonant one. Interestingly, we find it challenging to achieve stable trapping at or near the resonance of the BNAs, for example, using laser wavelengths of 785 nm for the $425\times 425\text{-nm}^2$ array. It is counterintuitive that the BNAs exhibit higher field enhancement,

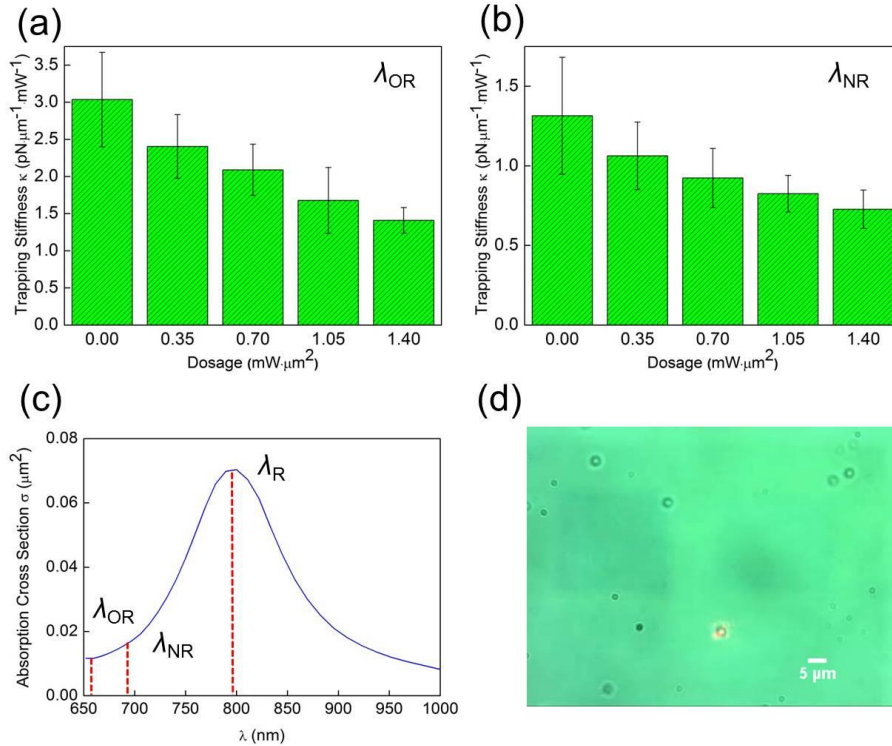


Figure 5. Experimental trapping stiffness. (a) and (b) are trapping stiffness plots for a 660 nm and 685 nm horizontally polarized input beam, respectively. The trapped particle is a 1 μm silica bead. (c) Simulated pBNA absorption cross-section in the upright orientation. $\lambda_{\text{NR}} = 791$ nm, $\lambda_{\text{NR}} = 685$ nm and $\lambda_{\text{OR}} = 660$ nm, respectively. (d) A representative frame from a movie of a trapped single particle using 500 μW of input power. The scale bar is 5 μm [16].

and thus higher gradient force amplification at these wavelengths, implying stronger optical forces. To explain this, it is useful to examine the extinction curves of the BNAs. In particular, the theoretical extinction at these wavelengths is higher than at 660 and 685 nm. However, a consequence of higher absorption is that heating produces a larger fluid force component than the increase of gradient force and forces along the optical axis, thereby destabilizing the trap.

3.2.5 Multiple Particle Plasmonic Optical Trapping

Figure 6 a,b,c,d,e show the time-lapse for multi-particle trapping of $1.0\ \mu\text{m}$ diameter silica bead using horizontally polarized, 660 nm illumination. The dark green-ish area represents the pillar bowtie nanoantenna arrays with 10 nm gap size and 525 nm spacing. A 0.25 NA objective provides $0.113\ \text{mW}/\mu\text{m}^2$ at its focal plane and successfully enables the manipulation of a group of more than 10 silica beads simultaneously. The successive images in Fig. 6 are taken at 5-second intervals when the movement of silica beads begins. The direction of movement is indicated by the red arrow as the particles move downward first and then horizontally to the left edge of pBNA region. Once the focused laser light exits the p-BNA area, the localized field of surface plasmons vanishes, and therefore the particles cease moving along and disperse away from their last trapping zone as in Fig. 6e.

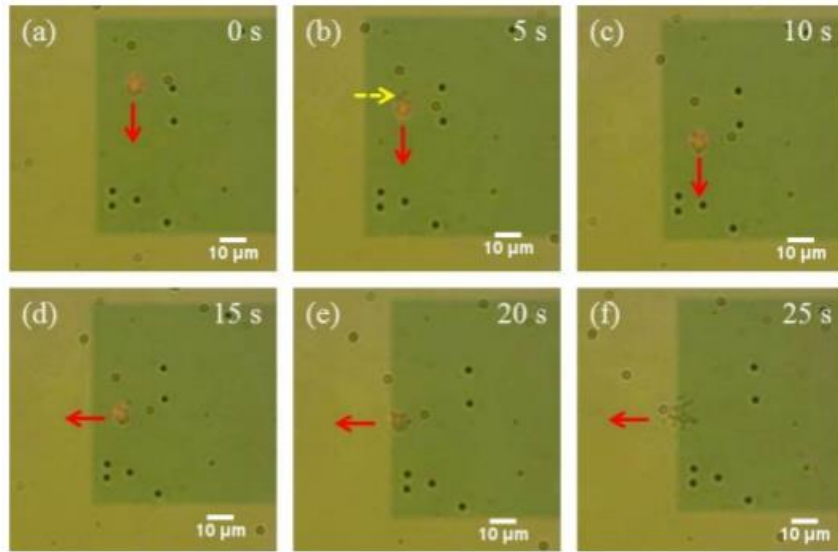


Figure 6. Plasmonic film-based nanotweezers. (a-f) Selected frames from a video of multiple particles trapping of $1\ \mu\text{m}$ diameter SiO_2 microspheres. The red spot indicates the leakage of the laser light and the scale bar is $10\ \mu\text{m}$ [16].

Owing to their plasmonic absorption, pillar bowtie nanoantennas generate strong local heating and thus induce thermal convection in fluid, which destabilizes the plasmonic trap and makes single-particle plasmonic trapping sometimes impossible if the convectional force overcomes the trapping force. In a multi-particle scenario like our experiment, the input power has been tuned to a low level (< 1 mW) where the convectional force, instead of being destructive, brings particles from distance and forms a cluster under the illumination. During the trapping state, this thermal convection also contributes to stabilizing the particles and constraining them inside the area excited by laser light. As illustrated in Fig. 7b, particles pointed out by the blue dashed arrow are about to escape the trapping zone of light red laser light area; however, in Fig. 7c they are pulled back and moving with other particles inside the cluster again.

Compared with other plasmonic trapping that utilizes BNAs, this approach in our experiment requires an objective of much smaller NA and hence less power density at focal plane in order to perform multi-particle plasmonic trapping. As p-BNA lacks heat-sinking effect of glass substrate compared to traditional BNA structure, its thermal convectional force aids to form a larger trapping area as a low NA objective can excite more p-BNAs under one illumination.

3.2.6 Optical Guiding with Writable Channels

The tenability of the trapping behavior of the pBNAs enables tailoring of the local potential energy landscape. One attractive application of the plasmonic film platform is optical trapping and guiding in pre-written channels. Mechanistically, this entails preferred trapping in an unexposed film area of the plasmonic film relative to regions that have previously been optically written and have the characteristic of lower trapping force and further detuned resonance. This interesting effect enables novel functionality compared to other nanotweezer systems, such as the formation of optofluidic channels “without walls”. To demonstrate these unique features, we first expose the film in an ambient-air environment using a $1.4 \text{ mW } \mu\text{m}^{-2}$ dosage with a focused beam to create predefined square wave trapping channels with a width of $\sim 5 \mu\text{m}$. The written channel is subsequently immersed in a water-based colloidal suspension of $1\text{-}\mu\text{m}$ diameter SiO_2 particles. As shown in Fig. 7, a portion of the channel is then illuminated with an approximately collimated, $15 \mu\text{m}$ diameter excitation beam (red circle in figure) obtained by focusing the 660 nm , horizontally polarized laser. We observe that particles are preferentially trapped in the predefined channels. This behavior is evident in Fig. 7a, which shows clusters of particles

trapped along a linear channel. Subsequently, we move the plasmonic film laterally and the particles are moved toward the left (Fig. 7a). As the cluster of particles hits the edge of the channel, due to the distributed exposed area on the left, the particles tend to cling to the side of the “wall” and relocate themselves along the vertical segment of the predefined channel as depicted in Fig. 7b. After all the particles are done distributing themselves in the vertical segment, we start moving our illumination upward to guide the particles to the exit of predefined channel as in Fig. 7b. Since the cluster of particles is confined in a narrow channel, some of the particles are stacked. As a result of unwanted mechanical vibration, a few particles diffuse down to the exposed area during the guiding process like in Fig. 7e. However, once these particles settle at the bottom of a channel, they are again dragged back to the channel by the local differences in gradient forces that are responsible for the preferential trapping along unexposed pBNA channels instead of exposed pBNA areas if we compare Fig. 7e and Fig. 7f [12].

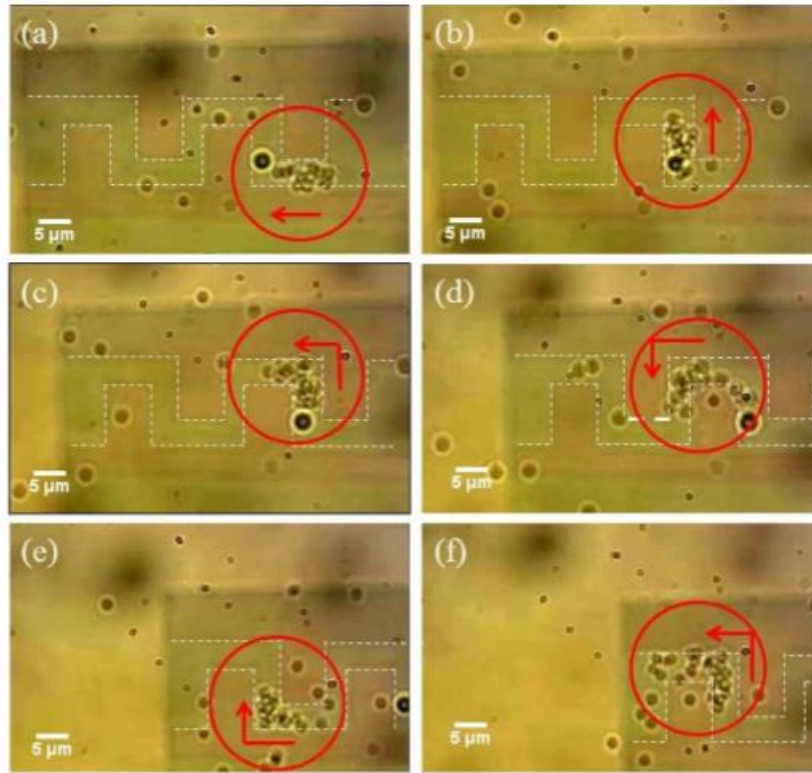


Figure 7. Plasmonic film-based particle guiding. (a-f) Selected frames from a video of guiding of 1 μm diameter SiO_2 in a predefined channel. The pre-written channel is the area outlined by the white dashed lines. The red circle indicates the illuminated region and the red arrow indicates the direction the illumination is moving. The scale bar is 5 μm [16].

3.3 Optical Film and Audio Recording

Aside from trapping, generally there is a heating effect associated with the plasmonic response with the gold layer. This heating effect is normally detrimental to plasmonic trapping as it destabilizes trapping by causing fluidic convection [11]. It turns out that by putting the BNAs on pillars, the heating effect makes the pBNAs much more sensitive to the input optical intensity, leading to photographic film effect. As elevated on 500 nm silica pillars, the heat conduction from the gold layer to the glass substrate is reduced significantly. Thus, with on-resonance illumination, 500 μW of optical power heats the BNAs up to 84 $^{\circ}\text{C}$ while same amount of optical power can easily heat the pBNAs up to 870 $^{\circ}\text{C}$ in air. Even with 100 μW of optical power, the temperature of the pBNAs can simply reach 214 $^{\circ}\text{C}$. The simulated temperature distributions for both BNA and pBNA are shown in Fig. 8. As the illumination dosage increases, the associated heating effect becomes more significant and thus the reflow of the metallic nanoparticle becomes more apparent. The reflow of the triangular bowtie nanoparticles on top of the pillars leads to the disappearance of their sharp tips, making the metallic nanoantennas more and more spherical, as shown in the SEM from Fig. 8.

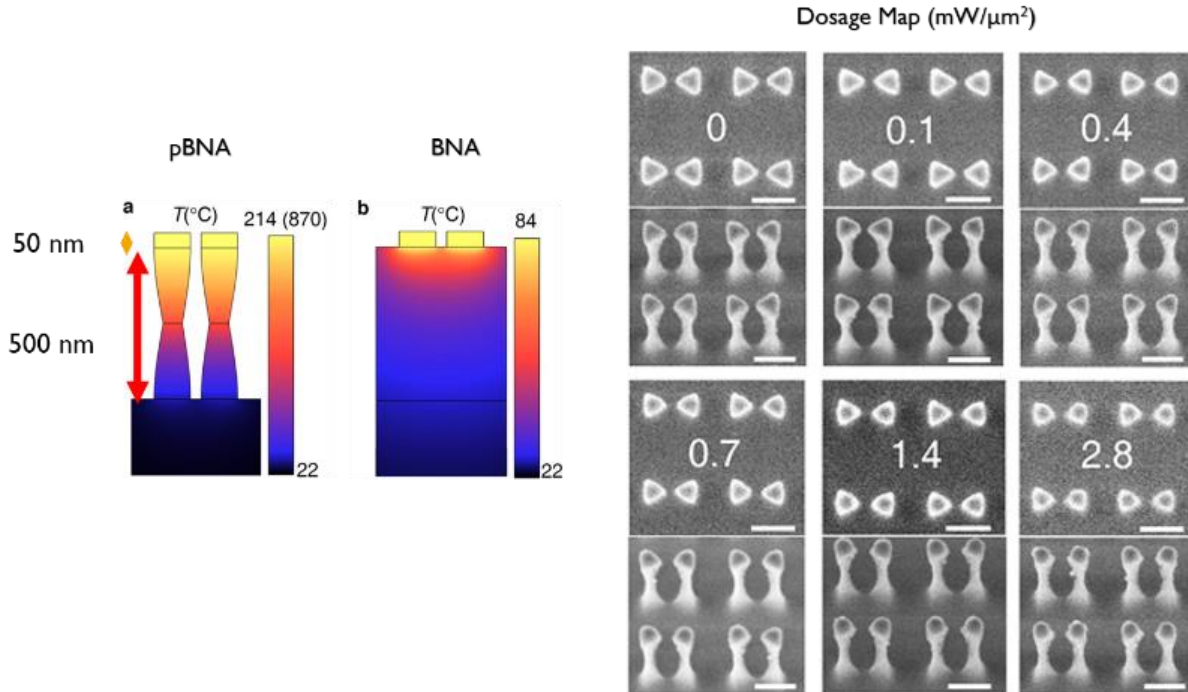


Figure 8. The pBNA has stronger heating effect such that the gold nanoparticles reflow and exhibits morphological changes, shown in the SEM. Scale bar, 200 nm [12].

The experimental setup used for audio recording and reading is detailed in Fig. 9a. A tunable Ti:sapphire laser is used to produce pulses at center wavelength of 780 nm and temporal width of 100 fs. The pulses are polarized along the long axis of the pBNAs. A high-speed scanning galvanometer mirror positioning system (Thorlabs GVS012) directs the pulses into the microscope system for optical beam steering. In the upright orientation, the pBNAs are illuminated from the substrate side. The audio recording and retrieval system are built around a customized inverted microscope (Olympus IX81) with a 0.6 numerical aperture (NA), collar-adjustable microscope objective (Olympus LUCPlanFLN 40 \times) used for illumination, which produces an approximately Gaussian intensity distribution with a full width at half maximum of 790 nm. On the other side of the sample, a 0.9 NA, microscope objective (Olympus MPlan LFN 100 \times) is used for dark-field imaging. A halogen lamp, white light source (Dolan Jenner, 190) is used to image the pBNAs onto a CMOS color camera (Thorlabs, DCC1645C), which is preceded by a laser-blocking band-pass filter.

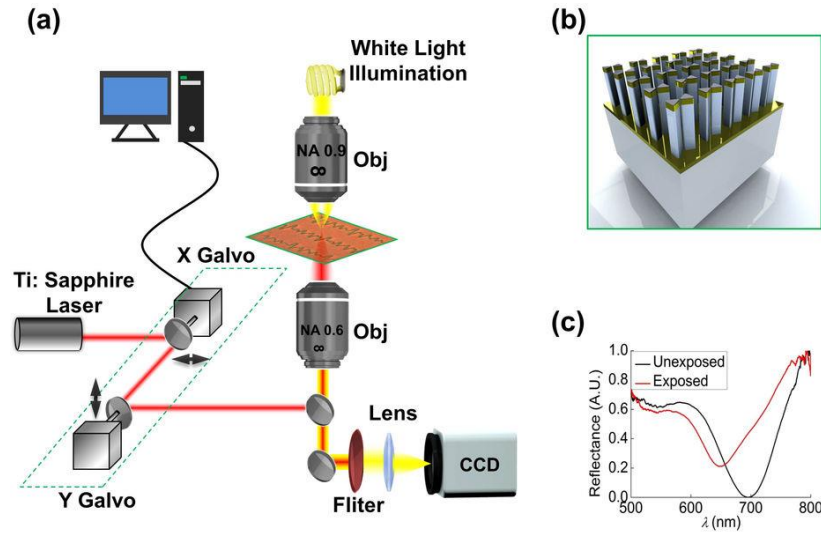


Figure 9. Schematic images of (a) experimental setup and (b) pBNAs. (c) Experimental spectral response of exposed and unexposed area of pBNAs showing the localized surface plasmon resonance shift [18].

The $80 \times 80 \mu\text{m}^2$ area of the plasmonic film comprises a 425×425 nm spaced array of pBNAs that are fabricated on top of a 25 nm thick ITO layer and a 400 μm thick SiO_2 substrate shown in Fig. 9b. Gold BNAs are sandwiched between an 8 nm thick Ni protective top layer and a 5

nm thick Cr adhesion bottom layer. The fabricated pBNAs have, on average, a 35 nm gap spacing and pillars with a height of 500 nm. The pBNAs are illuminated off-resonance at a wavelength of 780 nm. The functionality of plasmonic film for audio recording is derived from photothermally induced morphological changes in the Au particles. In order to observe visible changes with high contrast, 50 mW of average power is used for all experiments. The optical response of the unexposed and exposed region of the film is assessed by measuring the spectral reflectance, shown in Fig. 9c. A 60 nm of spectral shift is observed for the exposed area relative to the unexposed area.

Galvo operation for audio recording is programmed in Labview (National Instruments Corporation). The galvo driver is connected to a DAQ board (NI USB-6221) with the position of mirrors controlled by the output voltage. An audio signal stored in a computer is converted by Labview to an amplitude-varying voltage that drives the galvo mirrors. With a given sampling frequency of the original audio waveform, the number of points required to record the audio is determined. Given the 0.6 NA illumination objective, and the fact that the mechanical resolution of the galvo scan angle is $14\ \mu\text{rad}$, the distance between the sampling points on the plasmonic film is 45 nm. The normalized amplitude of the recorded audio is set as $6.5\ \mu\text{m}$. By transferring the audio information into voltages, waveform recording is enabled by laterally scanning the laser spot on the plasmonic film.

Dark-field imaging is used to record the image of the written waveform on the plasmonic film. In principle, bright-field imaging can also be used, but dark-field imaging provides high contrast images that facilitate post-processing. An RGB image is recorded by the color camera with the image background in red and the $\sim 790\ \text{nm}$ thick waveform in green. In the audio retrieving process, only the green element value is extracted from the RGB image. Note that a gradual color change in image pixels from green to red is observed at the edge of the waveform. However, through a standard edge detection approach, a single value can be determined for each lateral position.

Figure 10 provides a top view, scanning electron microscopy (SEM) image of the plasmonic film after a vertical-line illumination pattern (overlaid in red on the SEM). Visible morphological changes of the radius of curvature of each Au triangular tip, which in turn modifies the gap size, are observed. Not surprisingly, the gradual shape change along the

horizontal direction in the image is indicative of the intensity gradient distribution from a Gaussian beam. This results in a direct color change on the pBNAs. As shown in Fig. 10b, a line plot of the change in gap size versus transverse distance fits well with an intensity Gaussian profile of a 780 nm wavelength laser beam focused by a 0.6 NA objective. We employ basic image processing to convert the 2D pBNA image to a 1D time-varying audio signal.

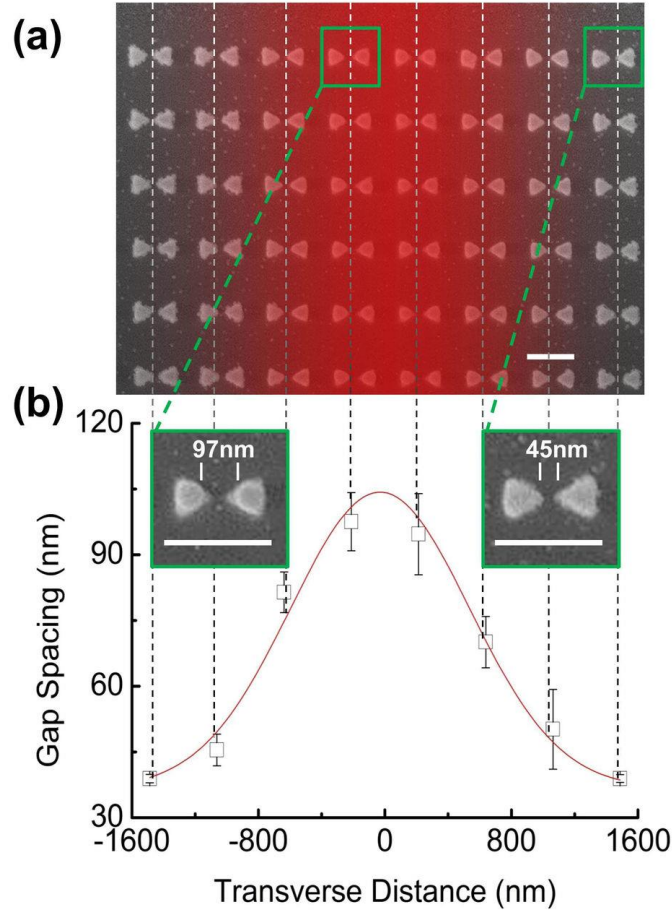


Figure 10. (a) Top view SEM images of an area of the pBNAs written with a Gaussian beam (shown in red over the SEM). (b) Line plot showing the change in gap spacing versus transverse position along the Gaussian beam shown in the SEM in (a). Insets from left to right are zoomed in SEM images for two representative pBNA pairs located at the center and edge, respectively. The scale bar represents 300 nm [18].

Figure 11 shows the results of writing 8 distinct musical notes onto the pBNAs. In this case, from Fig. 11a-h, we successfully record middle C (C_4), D, E, F, G, A, B and tenor C (C_5) on

the plasmonic film. As shown in the actual recorded images, each note is a single harmonic and the overall range of frequencies is from 261.63 Hz to 523.25 Hz. In our recording process, since each note is generated in a digital format with a standard sampling frequency of 44.1 kHz, one second of audio on the film corresponds to 44,100 illuminated points in a given segment. Similar to the musical keys on a keyboard, the notes can be played in a specified order to generate a desired sound. We demonstrate this type of “plasmonic keyboard” by taking the 8 recorded musical notes, and in the post-processing, arranging them to construct a short song.

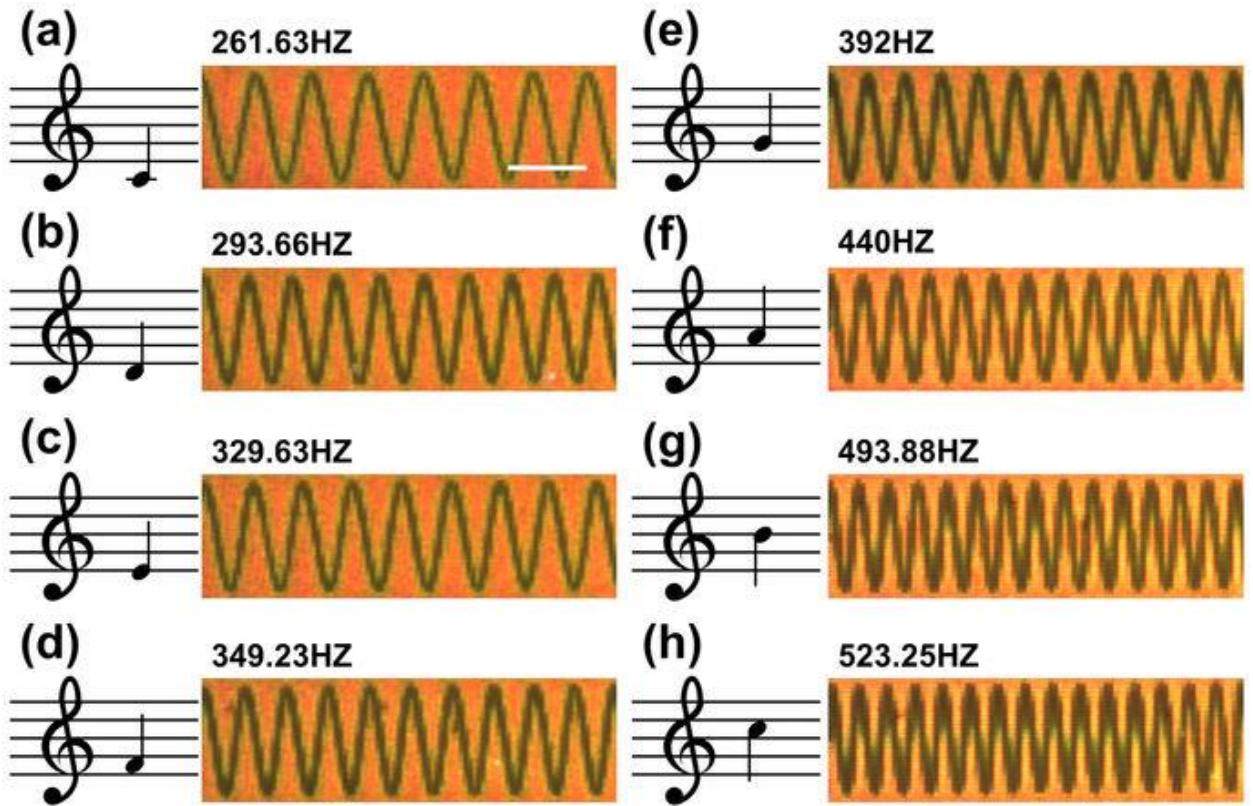


Figure 11. Dark-field images of pBNA regions, each showing one of the 8 recorded sinusoidal notes plotted (a–h); the corresponding musical notations are shown on the left as reference. The scale bar in (a) represents 10 μm and is the same for (b–h)[18].

Table 1. Correlation coefficient for 8 distinct notes.

	C ₄	D	E	F	G	A	B	C ₅
$\rho_{X,Y}$	0.995	0.994	0.990	0.983	0.985	0.983	0.974	0.932

To analyze the quality of the retrieved waveform read from the plasmonic film, we use the correlation coefficient $\rho_{X,Y} = \text{cov}(X,Y)/(\sigma_X \cdot \sigma_Y)$ to assess the quality of retrieval audio, where X and Y represent the original and retrieved signals, respectively, cov represents the covariance operation, and σ_X and σ_Y are the standard deviation of the corresponding original and retrieved signals. The correlation coefficients for the retrieved 8 notes in Fig. 11a-h are listed in Table 1. With an increase of the tone, a waveform with higher frequency oscillations is recorded within a unit area that causes aliasing. Thus, a decrease of the correlation coefficient is observed from C_4 to C_5 .

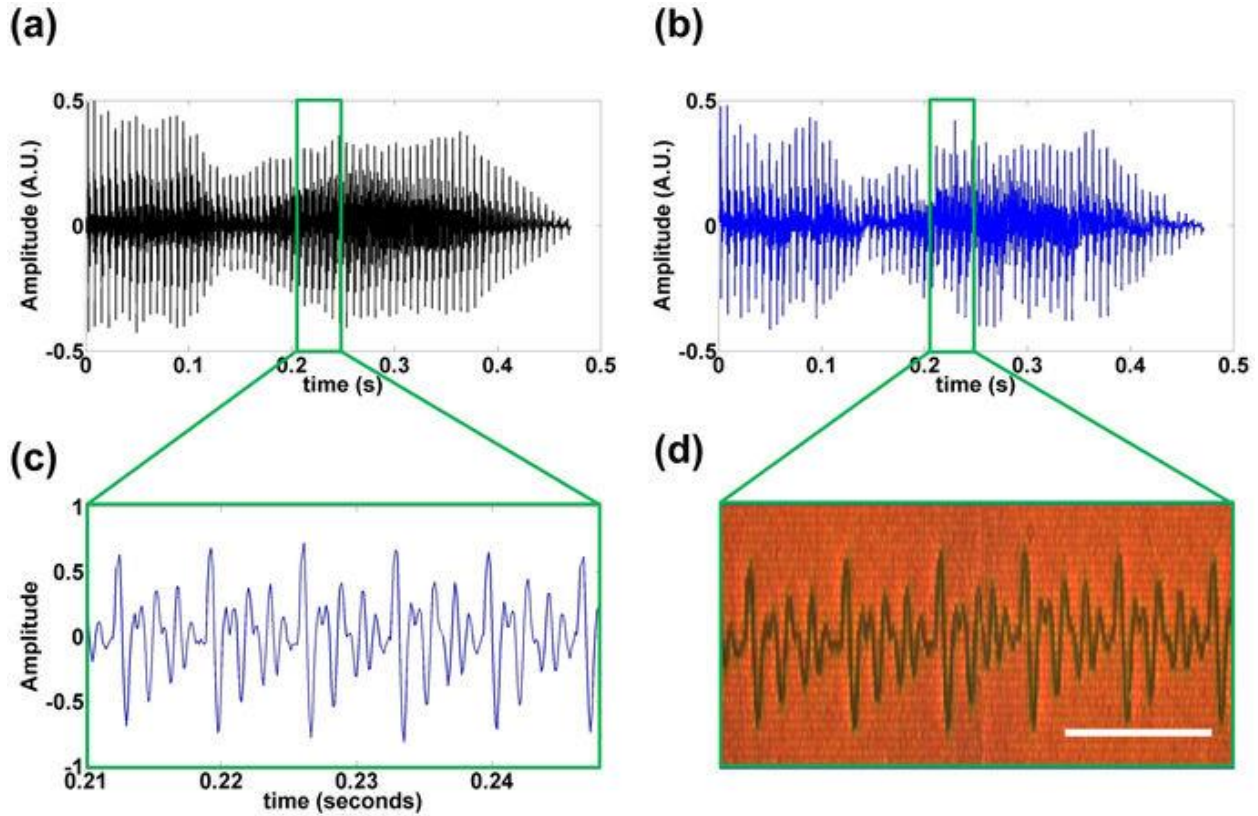


Figure 12. (a) Original audio data and (b) retrieved signal from the pBNAs. (c) is a representative zoomed-in segment from the original audio for time range $t = 0.21$ s to $t = 0.25$ s, and (d) is an image of corresponding, recorded, time segment on a region of the pBNAs. Scale bar represents $50 \mu\text{m}$ [18].

In a similar fashion, we next demonstrate the effectiveness of our approach in recording vocal (human voice) information. Here, a 470 ms recording of “hello” is recorded and Fig. 12a shows the original time-varying signal. To inspect more closely, we expand a short

segment of the audio file (~40 ms in duration) as shown in Fig. 12b. We compare the corresponding segment in Fig. 12c from the retrieved audio profile in Fig. 12d. Note that for improved quality, the spatial extent on the plasmonic film of this audio file is ~900 μm , which cannot fit into the total area of a single pBNA array ($80 \times 80 \mu\text{m}^2$). Thus, we use 7 additional arrays to stitch together the audio signal. However, due to the possible mismatch at the boundaries between the arrays, perfectly aligning the various pieces of the audio signal proves challenging, and we obtain a relatively low correlation coefficient of 0.342. Still, as proof-of-concept, it is clear from the audio that the plasmonic film can store audio (voice) information, as well.

To evaluate the capacity of the plasmonic film, we estimate the area required to store one second of audio information. For a standard recording process, the maximum amplitude is set as 13 μm and one second of audio is stored with a length requirement of 1962.2 μm . Therefore, an area of 0.0255 mm^2 is required on our plasmonic film for one second of audio storage. In comparison with magnetic tape as a standard analog data storage medium, an area of 1143 mm^2 is needed to store a one second audio signal. Thus, in the current form, the capacity of a unit area for plasmonic film is 5600 \times larger than the conventional magnetic tape.

Aside from the recording of a time-varying audio signal, we also demonstrate that the plasmonic film can be used to directly store the spectral information of an audio signal. This is achieved simply by taking the Fourier transform of the original time-domain signal and optically writing the corresponding amplitude and phase spectra on the plasmonic film. For demonstration purposes, we construct a 600 ms duration audio signal comprising of three notes (C₄, E and G), and transfer this information into the frequency domain. The notes are equally separated with a duration of 200 ms. Figure 13a, b are the respective amplitude and phase spectra for the transformed audio. We observe the 3 peaks in the amplitude spectrum, corresponding to the frequencies of the three recorded notes at 261.63 Hz, 329.63 Hz, and 392 Hz. The amplitude value elsewhere is close to zero and thus negligibly contributes to the retrieved signal. To get a better contrast, logarithmic plots of the amplitude spectrum are shown in Fig. 13. Based on these images, the retrieved spectra (shown in Fig. 13e,f) are obtained and then inverse Fourier transformed back to the time domain for audio playback.

Given that the spectrum is displayed on the plasmonic film, basic signal processing can be achieved by physically ablating unwanted frequency components on the nanostructure. In this case, we design a simple filter to block two of the low-frequency components (261.3 Hz and 329.63 Hz) on the plasmonic film, indicated by the two shaded rectangular regions (each spanning 25 Hz) in Fig. 13a. Thus, a scanning laser is used to physically ablate these two rectangular areas as shown in Fig. 13g. Note that the sharp edge of the filter is limited by diffraction only. Following the standard audio retrieval procedure, the filtered audio signal is reconstructed, with the value of the signal in the filtered region set to a null. The amplitude for the first 400 ms is close to zero.

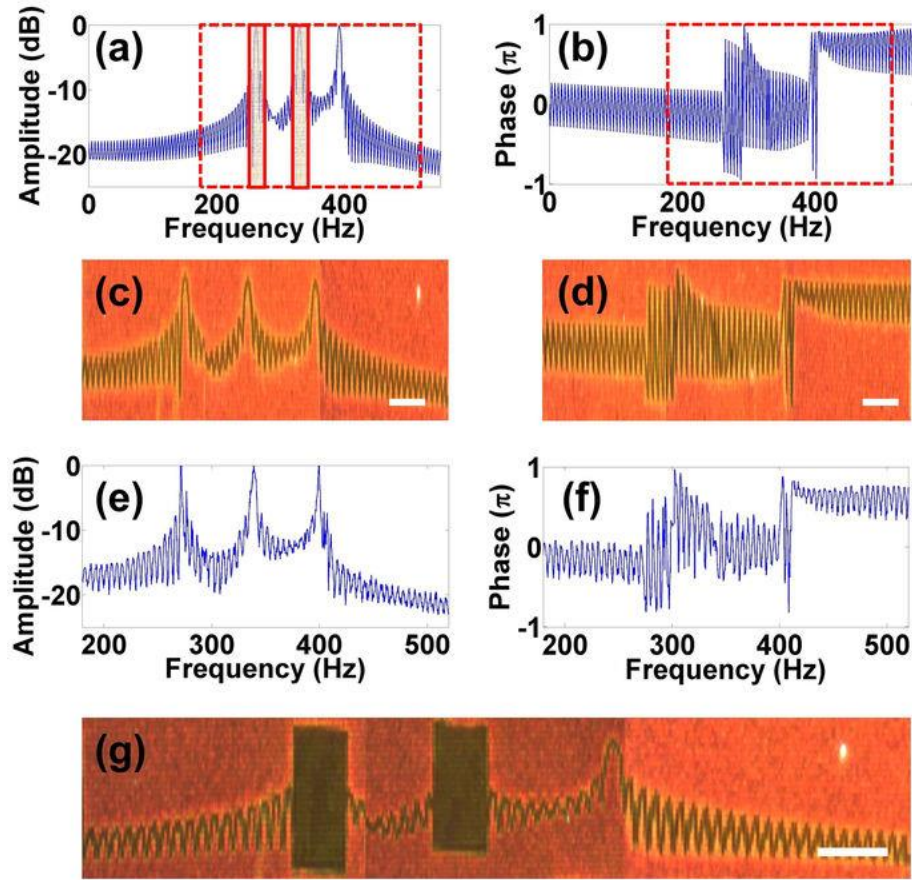


Figure 13. Original amplitude and phase spectra (a, b). The shaded rectangular regions indicate the two spectral windows, 250–275 Hz and 325–345 Hz, to be blocked. Dark-field image of recorded data from pBNAs (c, d) and corresponding retrieved amplitude and phase spectra from the recorded pattern (e, f). Recorded amplitude spectrum (g). The desired spectral windows are ablated. Scale bars represent 10 μm [18].

4. Conclusion

In summary, we demonstrate a new type of plasmonic nanotweezers on pillar-supported Au BNAs that offer trapping of multiple particles using lower input power densities due to increased heating in the structure. An interesting feature of the pBNAs is their ability to act like plasmonic film and record the near-field optical intensity. This characteristic offers the ability to shape the potential energy landscape in real time using low input power densities. To this point, we showed that unexposed plasmonic film with the smallest gap size demonstrates the largest trapping stiffness, and that a gradual decrease in stiffness is observed for increased input laser power dosage. We thus showed a route to fabricating optofluidic channels “without walls”. As part of our future work, we are currently exploring the lower limit of the NA that can be used for multiparticle trapping.

In addition, the pBNA structure exhibits stronger heating effect that can be used for application of optical film and audio recording. We showed that an audio signal can be stored either as a time-varying waveform or as frequency spectra. Simple signal processing is demonstrated by intentionally ablating the spectra in situ. Compared with conventional magnetic film for analog data storage, the storage capacity of pBNAs is around 5600 times larger. Furthermore, by employing emerging nanomanufacturing techniques, such as nanoimprint lithography [19], such technology could conceivably be mass produced and explored for potential data storage applications, including enhancing the niche, but still important, analog technology used in the area of archival storage (e.g., using microfiche); it also could be an important component in the development of on-chip, plasmonic-based information processing technologies [20]. Future improvements of this approach include using higher-numerical-aperture optics and pBNAs that are tuned to have a plasmonic response in the blue in order to increase the resolution in the writing.

References

- [1] L. Novotny and B. Hecht, *Principles of Nano-Optics*. Cambridge University Press, 2012.
- [2] V. Z. Anatoly and I. S. Igor, "Near-field photonics: surface plasmon polaritons and localized surface plasmons," *Journal of Optics A: Pure and Applied Optics*, vol. 5, p. S16, 2003.
- [3] S. A. Maier, *Plasmonics: Fundamentals and Applications*. 1st ed. Springer Science & Business Media, 2007.
- [4] L. Novotny and N. van Hulst, "Antennas for light," *Nature Photonics*, vol. 5, p. 83, 02/01/online 2011.
- [5] Y. Chu, E. Schonbrun, T. Yang, and K. B. Crozier, "Experimental observation of narrow surface plasmon resonances in gold nanoparticle arrays," *Applied Physics Letters*, vol. 93, p. 181108, 2008.
- [6] K. D. Ko, A. Kumar, K. H. Fung, R. Ambekar, G. L. Liu, N. X. Fang, *et al.*, "Nonlinear optical response from arrays of Au bowtie nanoantennas," *Nano Lett*, vol. 11, pp. 61-5, Jan 12 2011.
- [7] K. C. Neuman and S. M. Block, "Optical trapping," *Review of Scientific Instruments*, vol. 75, pp. 2787-2809, 2004.
- [8] B. J. Roxworthy, K. D. Ko, A. Kumar, K. H. Fung, E. K. C. Chow, G. L. Liu, *et al.*, "Application of plasmonic bowtie nanoantenna arrays for optical trapping, stacking, and sorting," *Nano Letters*, vol. 12, pp. 796-801, 2012/02/08 2012.
- [9] M. L. Juan, M. Righini, and R. Quidant, "Plasmon nano-optical tweezers," *Nature Photonics*, vol. 5, p. 349, 05/31/online 2011.
- [10] P. J. Reece, "Finer optical tweezers," *Nature Photonics*, vol. 2, p. 333, 06/01/online 2008.
- [11] B. J. Roxworthy, A. M. Bhuiya, S. P. Vanka, and K. C. Toussaint Jr, "Understanding and controlling plasmon-induced convection," *Nat Commun*, vol. 5, 01/21/online 2014.
- [12] B. J. Roxworthy, A. M. Bhuiya, V. V. G. K. Inavalli, H. Chen, and K. C. Toussaint, "Multifunctional plasmonic film for recording near-Field optical intensity," *Nano Letters*, vol. 14, pp. 4687-4693, 2014/08/13 2014.
- [13] S. Inasawa, M. Sugiyama, and Y. Yamaguchi, "Laser-induced shape transformation of gold nanoparticles below the melting point: The effect of surface melting," *The Journal of Physical Chemistry B*, vol. 109, pp. 3104-3111, 2005/03/01 2005.
- [14] R. Kofman, P. Cheyssac, A. Aouaj, Y. Lereah, G. Deutscher, T. Ben-David, *et al.*, "Surface melting enhanced by curvature effects," *Surface Science*, vol. 303, pp. 231-246, 1994/02/10/ 1994.
- [15] M. Ploschner, M. Mazilu, T. F. Krauss, and K. Dholakia, "Optical forces near a nanoantenna," *Journal of Nanophotonics* 4.1, p. 13, 2010
- [16] H. Chen, Q. Ding, B. J. Roxworthy, A. M. Bhuiya, and K. C. Toussaint, "Optical trapping with pillar bowtie nanoantennas," *Proc. SPIE*, pp. 91641M-91641M-7, 2014
- [17] J. S. Donner, G. Baffou, D. McCloskey, and R. Quidant, "Plasmon-assisted optofluidics," *ACS Nano*, vol. 5, pp. 5457-5462, 2011/07/26 2011.
- [18] H. Chen, A. M. Bhuiya, Q. Ding, and J. K. C. Toussaint, "Plasmon-assisted audio recording," *Scientific Reports*, vol. 5, p. 9125, 03/16/online 2015.
- [19] S. H. Ahn and L. J. Guo, "Large-area roll-to-roll and roll-to-plate nanoimprint lithography: A step toward high-throughput application of continuous nanoimprinting," *ACS Nano*, vol. 3, pp. 2304-2310, 2009/08/25 2009.

- [20] A. Silva, F. Monticone, G. Castaldi, V. Galdi, A. Alù, and N. Engheta, "Performing mathematical operations with metamaterials," *Science*, vol. 343, p. 160, 2014.